Journal of Neuroscience Methods 176 (2009) 104–111

Contents lists available at ScienceDirect

Journal of Neuroscience Methods

journal homepage: www.elsevier.com/locate/jneumeth

A method for localizing microelectrode trajectories in the macaque brain using MRI

Rishi M. Kalwani[a], Luke Bloy[b], Mark A. Elliott[b], Joshua I. Gold[a,*]

[a] Department of Neuroscience, University of Pennsylvania, 116 Johnson Pavilion, 3610 Hamilton Walk, Philadelphia, PA 19104-6074, United States
[b] Department of Radiology, University of Pennsylvania, Philadelphia, PA 19104, United States

ARTICLE INFO

Article history:
Received 30 November 2007
Received in revised form 25 August 2008
Accepted 25 August 2008

Keywords:
Magnetic resonance imaging
Primate
Microelectrode

ABSTRACT

Magnetic resonance imaging (MRI) is often used by electrophysiologists to target specific brain regions for placement of microelectrodes. However, the effectiveness of this technique has been limited by few methods to quantify in three dimensions the relative locations of brain structures, recording chambers and microelectrode trajectories. Here we present such a method. After surgical implantation, recording chambers are fitted with a plastic cylinder that is filled with a high-contrast agent to aid in the segmentation of the cylinder from brain matter in an MRI volume. The resulting images of the filled cylinder correspond to a virtual cylinder that is projected along its long axis – parallel to the trajectories of microelectrodes advanced through the recording chamber – through the three-dimensional image of the brain. This technique, which does not require a stereotaxic coordinate system, can be used to quantify the coverage of an implanted recording chamber relative to anatomical landmarks at any depth or orientation. We have used this technique in conjunction with Caret [Van Essen DC, Drury HA, Dickson J, Harwell J, Hanlon D, Anderson CH. An integrated software suite for surface-based analyses of cerebral cortex. J Am Med Inform Assoc 2001;8:443–59] and AFNI [Cox RW. AFNI: software for analysis and visualization of functional magnetic resonance neuroimages. Comput Biomed Res 1996;29:162–73] brain-mapping software to successfully localize several regions of macaque cortex, including the middle temporal area, the lateral intraparietal area and the frontal eye field, and one subcortical structure, the locus coeruleus, for electrophysiological recordings.

1. Introduction

Over the past decade and a half, magnetic resonance imaging (MRI) has become the *de facto* standard for anatomical localization of electrophysiological targets in the monkey brain (Alvarez-Royo et al., 1991; Asahi et al., 2003; Blaizot et al., 1999; Christensen et al., 1997; Freed et al., 2001; Glimcher et al., 2001; Nahm et al., 1994; Rebert et al., 1991; Saunders et al., 1990; Subramanian et al., 2005). In contrast to post-mortem histology, MRI is neither invasive nor terminal and thus can be taken at multiple times to both guide and confirm microelectrode placement. MRI also provides better spatial resolution and better contrast between gray and white matter compared to other imaging techniques that have been used, including conventional X-ray (Kennedy and Ross, 1980), ventriculography (X-ray combined with high-contrast agents injected into the cerebral ventricles: Clifton et al., 1975; Dubach et al., 1985; Ilinsky and Kultas-Ilinsky, 1982; Percheron, 1975; Percheron et al., 1996, 1986), pneumoencephalography (in which cerebrospinal fluid is drained from around the brain and replaced with air or gas in order to view the ventricles more clearly in an X-ray: Kraemer et al., 1978), computed tomography (CT, which provides a three-dimensional X-ray: Risher et al., 1997) and, more recently, ultrasonic imaging (Glimcher et al., 2001; Tokuno and Chiken, 2004; Tokuno et al., 2000).

MRI is typically used to help electrophysiological studies solve two distinct but related problems. The first is to determine the appropriate location and orientation to surgically implant a recording chamber to ensure access to a targeted brain region. A recent report introduced a novel set of methods that use MRI to solve this problem (Miocinovic et al., 2007). These methods involve a sophisticated software tool called Cicerone that can register MRI and CT images taken before surgery with each other and three-dimensional brain atlases. The registered images can then be used not only to plan the locations of recording chambers, craniotomies and microelectrodes, but also to visualize microelectrode trajectories and combine physiological and anatomical data. These features all rely on the ability to represent and visualize these disparate datasets in a common reference frame, the stereotaxic coordinate system of the monkey.

* Corresponding author. Tel.: +1 215 746 0028; fax: +1 215 573 9050.
E-mail address: jigold@mail.med.upenn.edu (J.I. Gold).

0165-0270/$ – see front matter © 2008 Elsevier B.V. All rights reserved.
doi:10.1016/j.jneumeth.2008.08.034

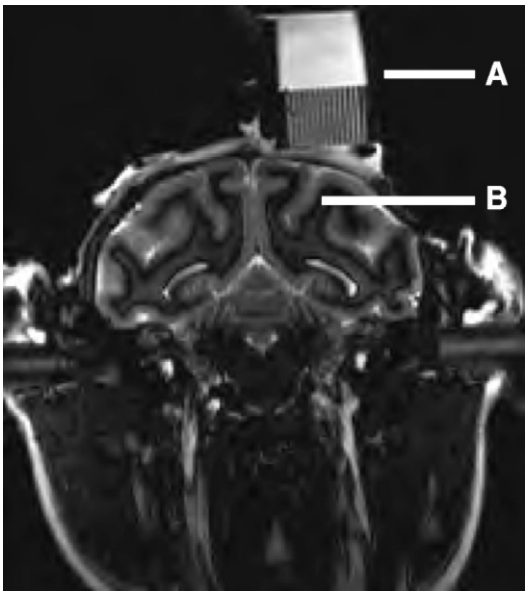

Fig. 1. Current qualitative method using MRI to determine recording chamber position relative to desired anatomical target(s). The image is a coronal section of the head and neck of a rhesus macaque (image courtesy Shadlen MN, University of Washington and HHMI). (A) Recording chamber and microelectrode grid (1 mm spacing; Crist Instruments, Inc., Hagerstown, MD) filled with saline. (B) Intraparietal sulcus. This is the primary anatomical landmark used to identify the location of the lateral intraparietal area (LIP), which is located on the lateral bank of the sulcus. Approximate electrode trajectories can be estimated by extending a particular grid hole ventrally through the image of the brain. However, this technique is limited to orientations within this plane of section.

The second problem is to verify that a recording chamber, once implanted, is positioned appropriately. A closely related issue is to determine where within the chamber microelectrodes should be placed and advanced to intercept the intended neural target. Fig. 1 shows a two-dimensional image corresponding to a single plane of section through the head of a monkey. From this image it is apparent that the recording chamber mounted to the skull is positioned approximately above the intraparietal sulcus. However, it is impossible to determine the three-dimensional trajectory of a microelectrode advanced from a particular location in the recording chamber relative to anatomical targets on or near the sulcus.

One effective solution to this problem has been to leave one or two microelectrodes in the brain during imaging (e.g., Paton et al., 2006; Liu and Richmond, 2000). The microelectrodes can be placed using the same microdrives or grid-based positioning systems that are used for electrophysiological recordings. Images can then be taken in a plane parallel to the microelectrode, providing a clear view of its trajectory relative to nearby brain structures. This image plane can also be used to estimate the depth of targeted structures relative to surface features like the bottom of the recording chamber. A particularly appealing feature of this technique is that it does not rely on the stereotaxic coordinate system but instead assesses directly the three-dimensional trajectory of the microelectrode relative to nearby brain structures.

Here we describe an extension of this method that replaces microelectrode placement with an image-processing algorithm to visualize the three-dimensional trajectory of the recording chamber through the brain. In addition to providing the same benefits as the microelectrode-placement method, our method is not invasive, does not require imaging in any particular plane and provides information about the complete coverage of the recording chamber relative to underlying brain areas. Our method can be used to identify the total volume of potential coverage within the brain for a particular recording chamber and within that coverage predict where a microelectrode should be placed for its trajectory to intercept an identified brain region.

2. Materials and methods

Four adult rhesus macaques (*Macaca mulatta*), two females (monkeys A and Z) and two males (monkeys C and W), were included in this study. The monkeys were cared for in accordance with the National Institutes of Health Guide for the Care and Use of Laboratory Animals, and all procedures were approved by the University of Pennsylvania Animal Care and Use Committee.

2.1. Surgeries

In a single surgical session, each monkey was implanted with a head-holding device and recording chamber(s) (Crist Instrument Co., Damascus, MD), both made of Cilux plastic and therefore suitable for MRI. The implant was constructed from Palacos® bone cement (Biomet Orthopedics, Inc., Warsaw, IN) mixed with antibiotics (Tobramycin and Vancomycin HCL). However, please note that we have experienced mixed results with this method in other animals (instability problems) and thus do not recommend it; all of our implants are now constructed from dental acrylic. Implants were secured to the skull using 8–12 ceramic (zirconia) screws (Ceramco, Inc., Center Conway, NH) placed around the outer perimeter.

2.2. Image acquisition

The monkey was fully sedated during image acquisition using a mixture of ketamine and medetomidine (reversed with antisedan). During the scan, the monkey was sometimes placed in an MRI-compatible stereotaxic apparatus (Kopf, Inc.). However, one advantage of the techniques described in this paper is that microelectrode trajectories can be computed relative to anatomical landmarks using only information contained in the image and not with respect to an extrinsic coordinate system. Therefore it is not necessary to use a stereotaxic frame, and in recent scans we have abandoned the practice. Instead, we used cushions to stabilize the monkey's head, which is less time consuming and eliminates soreness that can be caused by the eye, ear and mouth bars on the stereotaxic frame.

To produce high-contrast images of the cylinder defined by the recording chamber, a custom-made plastic cylinder filled with an aqueous solution of $CuSO_4$ (~1 mg/ml) was placed snugly inside the chamber (Fig. 2). The cylinder had a replaceable, tight-fitting cap with a pinhole that released a drop of liquid when it was pressed into place onto a solution-filled cylinder. It was made from CTFE plastic (McMaster-Carr) and measured ~7 cm length, 1.90 cm outer diameter and 0.125 cm thickness. The outer diameter was machined to be within a 0.01 cm tolerance of the inner diameter of the chamber. The length was somewhat arbitrary but in general should maximize the number of image slices through the cylinder (to minimize error in the cylinder fitting algorithm) that can be obtained in a single sequence that also includes the brain. We also found that lengths >~7 cm would sometimes make it awkward to position the head and cylinder(s) in the coil.

Monkeys were placed in a head first, prone position in a 1.5 T Siemens Sonata MRI scanner. A transmit/receive volume extremity coil was used. After using a brief, three-plane localizer for image positioning, high resolution, T1-weighted 3D-MPRAGE images were acquired in the magnet coronal plane with the following parameters: TE/TR/TI = 5.3/1720/930 ms, FOV = 140 mm × 127 mm, matrix = 192 × 174, slice thickness = 0.7 mm, slices = 160, acquisition time = 5 min. The resulting resolution was

Fig. 2. Recording chamber and plastic cylinder. The cylinder must fit snugly within the recording chamber so that the long axis of the cylinder is parallel to the long axis of the cylinder.

0.7 mm × 0.7 mm × 0.7 mm. The image sequence was typically acquired twice in 20-min blocks (five averages per block) resulting in a total scanning time of ~40 min. The interval between the two scans allowed us to check the monkey's position, level of sedation and vital signs at regular intervals. After the scan, offline motion correction was applied to the two MPRAGE images using SPM2 (http://www.fil.ion.ucl.ac.uk/spm/), and the mean motion correction image was used for further analysis.

2.3. Image processing

We developed image-processing software to compute from the MR image sequence the three-dimensional coordinates of the $CuSO_4$-filled cylinder and virtually project that cylinder along its long axis through the brain. The basic algorithm is depicted in Fig. 3. The MR imaging sequence through the head, implant and cylinder produces several planes of section that contain elliptical cross-sections of the cylinder. Because the cylinder is a rigid, uniform cylinder, the ellipses produced in parallel cross-sections are nearly identical (corrupted by noise and slight sampling differences). The center point of each ellipse is determined by first thresholding the image and then computing the center of mass of the above-threshold voxels. The average ellipse is computed by aligning the (non-thresholded) images to the ellipse center points, averaging the voxels and re-thresholding. A line is fit to the center points, representing the long axis of the recording chamber, and projected virtually through the three-dimensional image volume. At any given point along the line, the projection of the recording chamber is computed as the average cross-sectional ellipse centered on the line. The software was implemented as a plug-in to AFNI (Cox, 1996) and generates an overlying projection volume that is separate from the underlying MRI volume.

A series of steps was necessary to view our structural MRI data in relation to a specific brain atlas in Caret (Van Essen et al., 2001). First, the cortical volume was segmented to yield a binary volume whose edges represent the shape of the cortex. Second, this segmented volume was used to automatically generate a surface. Third, the surface was deformed to match the atlas using shared geographic landmarks and a differeomorphic deformation algorithm (Joshi and Miller, 2000). This procedure permitted us to simultaneously view a specific region of interest, our electrophysiological penetration sites and the cylinder projection onto a single hemisphere.

2.4. Electrophysiology

For monkeys Z and C, neural activity was used to identify the middle temporal (MT) and lateral intraparietal (LIP) areas. Activity was recorded using quartz-coated platinum–tungsten microelectrodes advanced using mini-matrix microdrives (Thomas Recording, Inc., Giessen, Germany). Spike waveforms were stored and sorted offline using a multi-channel acquisition processor (Plexon, Inc., Dallas, TX). Area MT was identified by finding neurons with contralateral receptive fields ~5–10° in diameter and consistent direction and speed tuning to a 99.9% coherence random-dot motion stimulus (Allman and Kaas, 1971; Dubner and Zeki, 1971; Zeki, 1974). Area LIP was identified by finding neurons with contralateral response fields and spatially tuned delay-period activity on a delayed-saccade task (Colby et al., 1996; Gnadt and Andersen, 1988).

For monkey W, neural activity was used to identify the locus coeruleus (LC). Activity was recorded using quartz-coated platinum–tungsten microelectrodes advanced using a NAN microdrive (Plexon, Inc., Dallas, TX). LC was identified based on physiological properties of nearby structures (e.g., auditory responses in the inferior colliculus, located dorsally to the LC along our electrode trajectory), waveform shape, phasic responses to surprising stimuli (e.g., a tap on the door of the recording booth), low-frequency continuous discharge and decreased activity during periods of drowsiness (Clayton et al., 2004; Rajkowski et al., 1998, 2004).

For monkey A, electrical microstimulation was used to identify area FEF (Bruce et al., 1985). Glass-coated tungsten microelec-

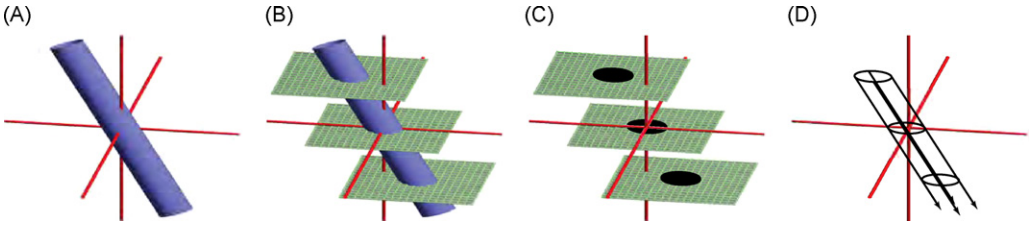

Fig. 3. Calculating the three-dimensional projection of the recording chamber. (A) Schematic of the cylinder (filled with an aqueous solution of $CuSO_4$) placed snugly in the recording chamber, shown in a three-dimensional Cartesian coordinate system (red axes). (B) The head, recording chamber and cylinder are all imaged together, including multiple planes of section through the cylinder. (C) All parallel planes of section that intersect the cylinder contain an image of an identical ellipse (planes that intersect <50% of the cross-sectional area on the ends of the cylinder are discarded). (D) These ellipses are projected virtually through the rest of the brain image along a line that connects their center points, representing the central long axis of the recording chamber.

trodes (Alpha Omega Engineering, Nazareth, Israel) were advanced using a NAN microdrive (Plexon, Inc., Dallas, TX). Area FEF was identified by finding sites at which saccadic eye movements with consistent (primarily contralateral) trajectories were evoked using <50 μA of current (0.25 ms biphasic pulses at 350–450 Hz for 60 ms).

Each site was classified as a "hit" or "miss" of the targeted brain region using two separate procedures. The first procedure used the above physiological criteria. The second procedure used anatomical criteria. For this procedure, the location of each site was expressed in the same coordinate system as the images using the two-dimensional position of the electrode within the recording chamber (using the view perpendicular to its long axis, as in Figs. 5–7G, rotated to align with penetration maps describing the electrode positions) and its depth relative to the dura. Once each site was expressed in this coordinate system, its position could be compared directly to the location of the targeted brain region defined in published atlases.

3. Results

Here we report on the effectiveness of this MRI-based technique for targeting specific brain regions for electrophysiological measurements. First we estimate the amount of error produced by the image-processing software. Then we describe results from electrophysiological experiments that used this technique to target three cortical areas (MT, LIP and FEF) and one brainstem structure (LC).

3.1. Estimates of error

Our image-processing algorithm is susceptible to errors that depend on the quality of the image. Noisy images make it difficult to distinguish the cylinder from the background. Low spatial resolution causes aliasing at the edges of the image of the cylinder. However, computer simulations suggest that for the quality of scans that we can easily expect to obtain in our ~40 min imaging sessions, errors in estimating microelectrode trajectories that arise from limitations in the images are <1 mm for depths of up to several cm (Fig. 4).

One type of error caused by low-quality images is in estimating the coverage of each cross-sectional ellipse image (see Section 2 and Fig. 4) relative to the actual $CuSO_4$-filled cylinder; that is, how much the image of the ellipse overlaps with the underlying cylinder. Fig. 4A and B shows that except for very noisy images (signal-to-noise ratio, or SNR, of <~1; in comparison, our cross-sectional images of the $CuSO_4$-filled cylinder had a SNR of >80, which we measured using ImageJ: http://rsb.info.nih.gov/ij/) and resolutions (a <~4-mm diameter cylinder imaged using 0.7-mm voxels; in comparison, our cylinders had an inner diameter of ~17 mm), coverage errors are predicted to be in most cases <3%.

A second type of error is in estimating the center of each cross-sectional ellipse image. Fig. 4C and D shows that reasonable ranges of SNR and resolution produce errors that are predicted to centered on zero and with a variability that is substantially smaller than the resolution of the image (standard deviations of the estimates of the center points were typically <0.1 mm for a 0.7-mm isotropic voxel size). However, even small errors in the estimates of the centers of the cross-sectional ellipses become magnified in the estimate of the location of the long axis of the recording chamber as it is projected in depth away from the sampled ellipses. This effect can be reduced by improving the estimate of the center point (Fig. 4E) or increasing the number of cross-sectional ellipses used to compute the projection (Fig. 4F).

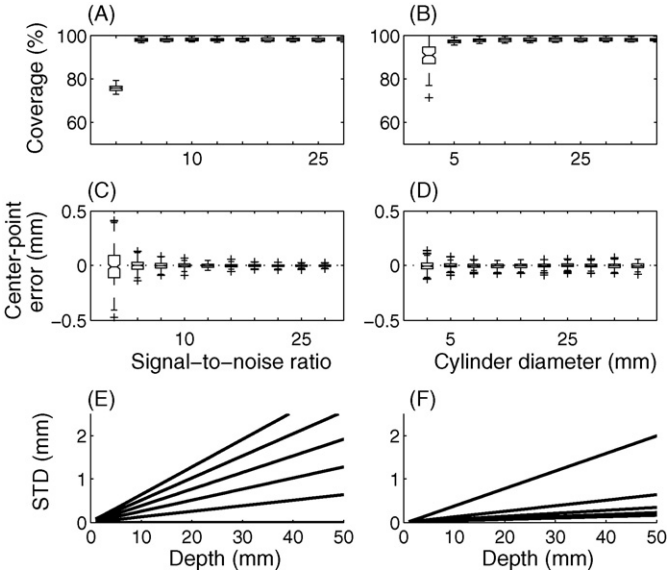

Fig. 4. Estimates of error. All errors were stimulated by comparing a high-resolution (0.01 mm isotropic voxels) image of an ellipse of a random aspect ratio (between 1 and 2.5) and orientation (between 0° and 180°) to a sampled, corrupted version of the same ellipse (0.7 mm isotropic voxels; $n = 100$ iterations per condition). (A) Box-and-whisker plot (center lines are medians; boxes are interquartile ranges; lines extend to the most extreme values within 1.5 times the interquartile range; crosses are outliers) of coverage (percent of the high-resolution image covered by the sampled image) as a function of the signal-to-noise ratio (SNR) of the sampled image. For these simulations, cylinder diameter = 20 mm. (B) Box-and-whisker plot of coverage as a function of cylinder diameter; SNR = 20. (C) Error in the estimate of the center point of the high-resolution ellipse in one dimension (estimated using the sampled image) as a function of SNR; cylinder diameter = 20 mm. (D) Error in the estimate of the center point of the high-resolution ellipse in one dimension as a function of cylinder diameter; SNR = 20. (E) Standard deviation of the estimated location of the long axis of the cylinder corresponding to the high-resolution ellipses as a function of depth from the sampled ellipses. Lines correspond to different standard deviations in the estimates of the centers of the sampled ellipses (bottom-to-top are 0–0.1 mm in increments of 0.02). (F) Standard deviation of the estimated location of the long axis of the high-resolution cylinder as a function of depth from the sampled ellipses. Lines correspond to different numbers of sampled ellipses (top-to-bottom are 2–10 in increments of 2). (E and F) Errors in the estimates of the centers of the sampled ellipses increase with increasing depth.

3.2. Targeting cortical areas MT, LIP and FEF

Stereotaxic surgeries were performed on monkey Z to target area MT (Fig. 5), on monkey C to target area LIP (Fig. 6) and on monkey A to target area FEF (Fig. 7). MRIs were acquired several weeks after surgery. Our image-processing software was then used to determine if the recording chambers were placed appropriately and, if so, where to place our microelectrodes within the chambers and how far to advance them to target the appropriate brain region. Because all three regions have been characterized extensively (for reviews, see Andersen and Buneo, 2002; Britten, 2001; Colby and Goldberg, 1999; Schall, 2002), we could then use known physiological properties to help confirm the effectiveness of this technique.

Panel A of Figs. 5–7 shows the three-dimensional orientation of the recording chamber and $CuSO_4$-filled cylinder (pseudocolored for clarity) relative to the cranium of each monkey, displayed using the Volume Rendering Plugin of the AFNI software package (Analysis of Functional NeuroImages; Cox, 1996). This view provides an external visualization of the cylinder trajectory relative to the head. Our goal was to view this trajectory relative to the internal anatomical features of the brain of each monkey.

The internal projections of the cylinders were visualized using automated segmentation and surface reconstruction tools in the

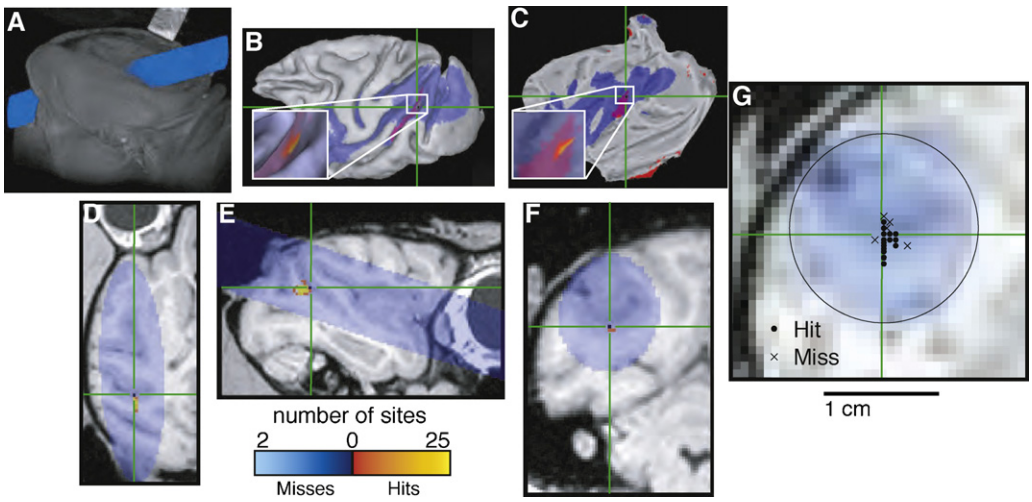

Fig. 5. Localizing area MT. In each panel, blue indicates cylinder coverage (diameter = 1.65 cm), green crosshairs and red spots in (B) and (C) indicate the predicted location of MT determined by registering the images to a publicly available atlas (Lewis and Van Essen, 2000; Van Essen and Dierker, 2007) and color codes shown at bottom indicate the number of recording sites at a given location classified as a "hit" or "miss" of MT based on physiological properties, including tuning for the direction of visual motion and restricted receptive fields in contralateral space (Allman and Kaas, 1971; Dubner and Zeki, 1971; Zeki, 1974). (A) Volume render showing external surfaces of the head and recording chamber. (B) Surface reconstruction of the left cortical hemisphere. (C) Flat map of the left cortical hemisphere. (D) Horizontal section. (E) Sagittal section. (F) Coronal section. (G) Section taken perpendicular to the long axis of the recording chamber at a depth corresponding to the location of MT. Circles indicate penetrations that included at least one recording site that was classified as MT based on physiological properties; crosses indicate penetrations with no sites that were classified as MT. (B) and (C) were generated using Caret (Van Essen et al., 2001). (A) and (D–G) were generated using AFNI (Cox, 1996). (For interpretation of the references to color in this figure legend, the reader is referred to the web version of the article.)

Caret-SureFit Software Suite (Van Essen et al., 2001; note that SureFit's features are now incorporated into Caret). Structural MRIs from each monkey were segmented and then reconstructed into a specific surface representation. This representation is essentially a wire-frame tessellation whose nodes sit on the edge of the segmentation and whose surface topology is defined by the links between nodes. The raw surface, which appears blocky because of the cubic voxels of the segmentation, is smoothed to generate an acceptable fiducial surface (Van Essen et al., 2001).

Each monkey's surface reconstruction was then used to visualize its cylinder projection(s). Each projection was mapped from the MRI volume onto the surface using a Caret-SureFit algorithm that accounts for local surface orientation when mapping volumetric data onto the surface (Van Essen et al., 2001). Each monkey's spe-

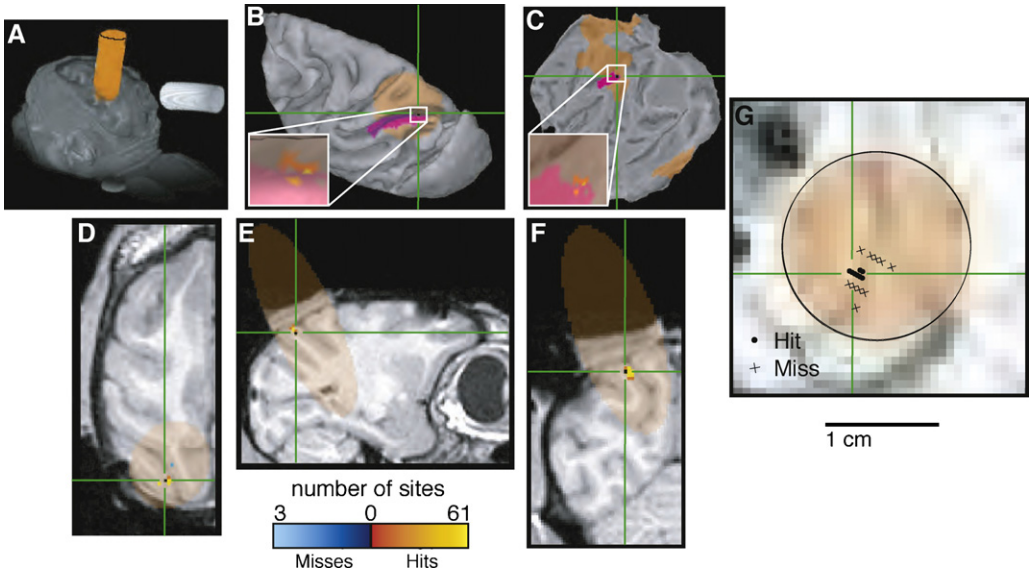

Fig. 6. Localizing area LIP. In each panel, orange indicates cylinder coverage (diameter = 1.65 cm), green crosshairs and purple spots in (B) and (C) indicate the predicted location of LIP determined by registering the images to a publicly available atlas (Lewis and Van Essen, 2000; Van Essen and Dierker, 2007) and color codes shown at bottom indicate the number of recording sites at a given location classified as a "hit" or "miss" of LIP based on physiological properties, including spatially selective visual, delay and oculomotor responses (Gnadt and Andersen, 1988; Colby et al., 1996). (A) Volume render showing external surfaces of the head and recording chamber. (B) Surface reconstruction of the left cortical hemisphere. (C) Flat map of the left cortical hemisphere. (D) Horizontal section. (E) Sagittal section. (F) Coronal section. (G) Section taken perpendicular to the long axis of the recording chamber at a depth corresponding to the location of LIP. Circles indicate penetrations that included at least one recording site that was classified as LIP based on physiological properties; crosses indicate penetrations with no sites that were classified as LIP. (B) and (C) were generated using Caret (Van Essen et al., 2001). (A) and (D–G) were generated using AFNI (Cox, 1996). (For interpretation of the references to color in this figure legend, the reader is referred to the web version of the article.)

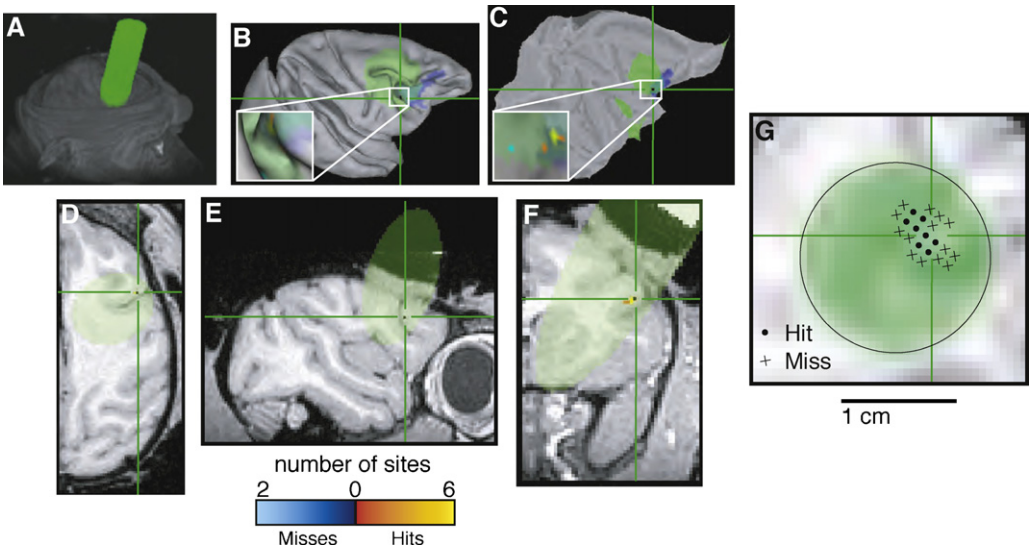

Fig. 7. Localizing area FEF. In each panel, green indicates cylinder coverage (diameter = 1.65 cm), green crosshairs and blue spots in (B) and (C) indicate the predicted location of FEF determined by registering the images to a publicly available atlas (Lewis and Van Essen, 2000; Van Essen and Dierker, 2007) and color codes shown at bottom indicate the number of recording sites at a given location classified as a "hit" or "miss" of FEF based on physiological properties, including the ability to evoke saccadic eye movements with electrical microstimulation using <50 μA of current (Bruce et al., 1985). (A) Volume render showing external surfaces of the head and recording chamber. (B) Surface reconstruction of the right cortical hemisphere. (C) Flat map of the right cortical hemisphere. (D) Horizontal section. (E) Sagittal section. (F) Coronal section. (G) Section taken perpendicular to the long axis of the recording chamber at a depth corresponding to the location of the FEF. Circles indicate penetrations that included at least one recording site that was classified as FEF based on physiological properties; crosses indicate penetrations with no sites that were classified as FEF. (B) and (C) were generated using Caret (Van Essen et al., 2001). (A) and (D–G) were generated using AFNI (Cox, 1996). (For interpretation of the references to color in this figure legend, the reader is referred to the web version of the article.)

cific surface was then mapped to a surface-based atlas in order to view the relative positions of the projection and the monkey's cortical area of interest (panels B and C of Figs. 5–7). MRI sections were obtained using AFNI to visualize cylinder projections relative to internal features (panels D–G of Figs. 5–7). These sectional images could be registered to the corresponding specific surface to identify the locations of the cortical areas of interest from the mapped atlases (green crosshairs; Van Essen and Dierker, 2007). A particularly useful view is perpendicular to the long axis of the recording chamber, which permits visualization of brain regions in the frame of reference used to position the microelectrodes within the cylinder (panel G of Figs. 5–7).

Expressing the MR images and microelectrode positions into a common frame of reference also allowed us to quantify their overlap. The insets of panels B and C in Figs. 5–7 show the anatomical relationship between each targeted brain region and the corresponding recording sites, each of which was defined as a "hit" or "miss" separately using anatomical and physiological criteria (see Section 2). Table 1 quantifies these relationships. For all three brain regions, the majority of sites were defined in a congruent fashion using anatomical and physiological criteria (82.8% of MT sites, 57.5% of LIP sites and 76.9% of FEF sites were defined as hits or misses based on both physiological and anatomical criteria). Most of the incongruently defined sites were physiological hits but anatomical misses (15.5% of MT sites, 41.3% of LIP sites and 23.1% of FEF sites), possibly reflecting individual variability in the exact location of these cortical areas (Lewis and Van Essen, 2000; Wagman et al., 1975).

Table 1
Comparison of anatomically and physiologically defined recording sites

Targeted cortical area		*P*+	*P*−
MT	*A*+	339 (81.1%)	7 (1.7%)
	A−	65 (15.5%)	7 (1.7%)
LIP	*A*+	157 (48.0%)	4 (1.2%)
	A−	135 (41.3%)	31 (9.5%)
FEF	*A*+	9 (34.6%)	0 (0.0%)
	A−	6 (23.1%)	11 (42.3%)

P+/*P*−: sites defined physiologically as a hit (+) or miss (−) of the given area. *A*+/*A*−: sites defined anatomically as a hit (+) or miss (−) of the given area. Each entry is *n* (%).

3.3. Targeting the LC in the brainstem

Similar methods were used to target recording sites in the LC, located in the pons along the lateral edge of the IVth ventricle. However, the Caret-SureFit brain-mapping software does not interface with atlases of subcortical structures as it does with surface-based atlases. Therefore, instead of targeting LC using atlas-based coordinates we identified two nearby structures, the inferior colliculus and IVth ventricle, easily seen in the images (Fig. 8). We found physiologically defined LC recordings sites within a few mm of their expected locations based on these MRI-based estimates.

4. Discussion

We developed a simple technique for determining the three-dimensional trajectories of recording microelectrodes placed in the brain along the long axis of a recording chamber attached to the skull. The technique uses MRI, which has become readily available to most researchers who conduct electrophysiological experiments in non-human primates, but does not require long scans (a typical imaging session for us lasted 40 min), high-powered magnets (most of our imaging was done using a 1.5 T scanner) or a stereotaxic apparatus. Briefly, a cylinder filled with a high-contrast agent ($CuSO_4$-doped water) is placed snugly in the recording chamber and is imaged along with the brain. Multiple planes of section through the cylinder produce images of ellipses that are used to reconstruct the three-dimensional structure of the cylinder. This reconstructed cylinder can then be projected virtually through the image of the brain and compared to the locations of specific brain

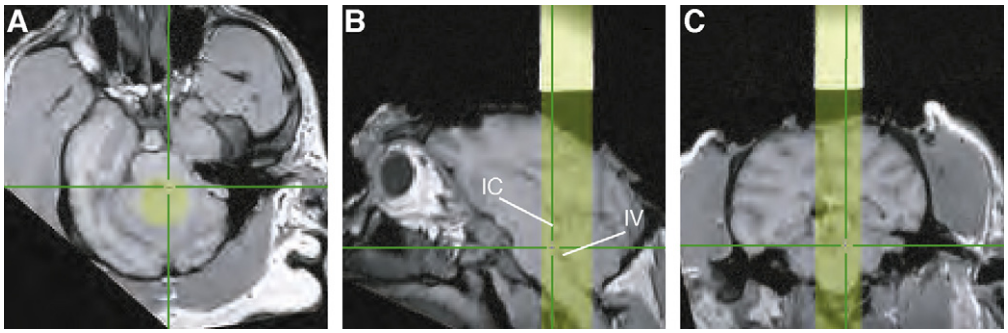

Fig. 8. Localizing the LC. In each panel, yellow indicates cylinder coverage (diameter = 1.65 cm), green crosshairs indicate the estimated location of LC determined by physiological properties of neurons recorded at that site, including waveform shape, phasic responses to surprising stimuli, low-frequency continuous discharge and decreased activity during periods of drowsiness (Clayton et al., 2004; Rajkowski et al., 1998, 2004). (A) Section taken perpendicular to the long axis of the recording chamber at a depth corresponding to the estimated location of the LC. (B) Sagittal section. IC, inferior colliculus; IV, IVth ventricle. (C) Coronal section. (For interpretation of the references to color in this figure legend, the reader is referred to the web version of the article.)

regions estimated from published atlases (see Figs. 5–7) or known anatomical landmarks (Fig. 8).

This technique, which is intended to complement methods that use a stereotaxic reference frame to visualize anatomy and recording hardware (Miocinovic et al., 2007), has given us two distinct advantages. First, it allows us to confirm whether or not the recording chamber, typically placed using stereotaxic methods during surgery, is positioned appropriately. Stereotaxic procedures define the location of any position in the brain relative to a known coordinate system (Horsely, 1908). Although stereotaxic procedures yield consistent results in smaller animals, neuroanatomical structures in larger mammals, such as macaques, are just roughly aligned with cranial landmarks (Glimcher et al., 2001; Percheron and Lacourly, 1973) and are subject to substantial inter-animal variability (Wagman et al., 1975). Thus, this method is especially imprecise for monkey neurophysiology (Aggleton and Passingham, 1981; Olzewski, 1952; Percheron, 1975; Percheron and Lacourly, 1973; Saunders et al., 1990; Subramanian, 2001; Subramanian et al., 2005) and requires verification and possible adjustment. Our method avoids the stereotaxic reference frame altogether and instead compares directly the location and orientation of the recording chamber and underlying brain structures.

Second, this technique allows us to determine where to place our microelectrodes within the recording chamber and how far to advance them in depth to target the brain area of interest. Although finding an appropriate recording site still requires a certain amount of searching, this technique has greatly reduced the amount of time needed to do so. Using this technique we have expeditiously located several regions of the cerebral cortex (MT, LIP, and FEF) and one brainstem structure (LC). In general, finding appropriate sites now takes us days instead of weeks of searching.

The precision of this technique depends on several factors. Our simulations show that the image-processing algorithm is susceptible to errors produced by low SNR or spatial resolution of the MR images (Fig. 4). However, for reasonable values of SNR (>10) and resolution (0.7-mm isotropic voxels for a ~20-mm diameter cylinder) that we were able to obtain easily in our images, our image-processing algorithm will provide >95% coverage of the recording chamber and an unbiased estimate of its long axis to within <1 mm up to ~2 cm in depth. This amount of error seems likely to be relatively small compared to other, less predictable sources of error that will influence the ability to use these images to target specific brain regions, including: (1) individual variability in the locations of specific brain regions relative to identifiable anatomical landmarks, particularly in larger animals like macaques (Wagman et al., 1975); (2) movement of the brain relative to the skull (and recording apparatus); (3) variability in the day-to-day placement of microelectrodes within the recording chamber (a problem that can be minimized by using a fixed grid for guiding microelectrode placement, at the expense of spatial resolution), and (4) microelectrode trajectories that do not travel exactly parallel to the long axis of the recording chamber (because of flexible microelectrodes that can bend unpredictably when traveling through tissue, for example). These additional sources of variability make it difficult to envision fundamental improvements to the precision of this kind of MRI-based technique even if the SNR and spatial resolution were to improve substantially.

Our application is acute, extracellular recordings in the cerebral cortex of awake monkeys. The size of the monkey brain (~60–70 mm in length; Martin and Bowden, 1996) and our recording chambers (19 mm inner diameter) and the size (at least several mm across) and depth of the targeted brain regions (<~10 mm deep for cortical areas MT, LIP, and FEF; ~40 mm deep for LC; Martin and Bowden, 1996; Stanton et al., 1989; Lewis and Van Essen, 2000) all contribute to the appropriateness of this technique, which provides an estimate of microelectrode trajectories with a precision of <~1 mm. Smaller brains, recording chambers or targeted brain regions would all pose stronger challenges to this or any other technique that attempts to determine precisely the microelectrode trajectories that would intersect the chosen targets.

Acknowledgements

We thank Fred Letterio, Jean Zweigle, Donna Dierker and Erin Reid for technical assistance. Supported by EY015260, MH062196, the McKnight Foundation, the Burroughs-Wellcome Fund and the Sloan Foundation (RK and JG) and RR02305 (LB and ME).

References

Aggleton JP, Passingham RE. Stereotaxic surgery under X-ray guidance in the rhesus monkey, with special reference to the amygdala. Exp Brain Res 1981;44:271–6.
Allman JM, Kaas JH. Representation of the visual field in striate and adjoining cortex of the owl monkey (*Aotus trivirgatus*). Brain Res 1971;35:89–106.
Alvarez-Royo P, Clower RP, Zola-Morgan S, Squire LR. Stereotaxic lesions of the hippocampus in monkeys: determination of surgical coordinates and analysis of lesions using magnetic resonance imaging. J Neurosci Methods 1991;38:223–32.
Andersen RA, Buneo CA. Intentional maps in posterior parietal cortex. Annu Rev Neurosci 2002;25:189–220.
Asahi T, Tamura R, Eifuku S, Hayashi N, Endo S, Nishijo H, et al. A method for accurate determination of stereotaxic coordinates in single-unit recording studies in monkeys by high-resolution three-dimensional magnetic resonance imaging. Neurosci Res 2003;47:255–60.
Blaizot X, Meguro K, Le Mestric C, Constans JM, Luet D, Baron JC, et al. Combined use of T1-weighted MRI and MRA for stereotaxic lesioning of the nonhuman primate brain: application to the rhinal cortex. Exp Brain Res 1999;126:31–40.
Britten KH. Extrastriate cortex: a signature of perception grows. Curr Biol 2001;11:R744–6.

Bruce CJ, Goldberg ME, Bushnell MC, Stanton GB. Primate frontal eye fields. II. Physiological and anatomical correlates of electrically evoked eye movements. J Neurophysiol 1985;54:714–34.
Christensen GE, Joshi SC, Miller MI. Volumetric transformation of brain anatomy. IEEE Trans Med Imaging 1997;16:864–77.
Clayton EC, Rajkowski J, Cohen JD, Aston-Jones G. Phasic activation of monkey locus ceruleus neurons by simple decisions in a forced-choice task. J Neurosci 2004;24:9914–20.
Clifton DK, Ochsner AJ, Uno H, Norman RL, Spies HG. Radiographic approach to stereotaxic surgery in rhesus monkeys. Physiol Behav 1975;14:103–7.
Colby CL, Duhamel JR, Goldberg ME. Visual, presaccadic, and cognitive activation of single neurons in monkey lateral intraparietal area. J Neurophysiol 1996;76:2841–52.
Colby CL, Goldberg ME. Space and attention in parietal cortex. Annu Rev Neurosci 1999;22:319–49.
Cox RW. AFNI: software for analysis and visualization of functional magnetic resonance neuroimages. Comput Biomed Res 1996;29:162–73.
Dubach MF, Tongen VC, Bowden DM. Techniques for improving stereotaxic accuracy in *Macaca fascicularis*. J Neurosci Methods 1985;13:163–9.
Dubner R, Zeki SM. Response properties and receptive fields of cells in an anatomically defined region of the superior temporal sulcus in the monkey. Brain Res 1971;35:528–32.
Freed CR, Greene PE, Breeze RE, Tsai WY, DuMouchel W, Kao R, et al. Transplantation of embryonic dopamine neurons for severe Parkinson's disease. N Engl J Med 2001;344:710–9.
Glimcher PW, Ciaramitaro VM, Platt ML, Bayer HM, Brown MA, Handel A. Application of neurosonography to experimental physiology. J Neurosci Methods 2001;108:131–44.
Gnadt JW, Andersen RA. Memory related motor planning activity in posterior parietal cortex of macaque. Exp Brain Res 1988;70:216–20.
Horsely VCR. The structure and functions of the cerebellum examined by a new method. Brain 1908;31:1–80.
Ilinsky IA, Kultas-Ilinsky K. Stereotactic surgery in the rhesus monkey (*Macaca mulatta*) utilizing intracerebral landmarks. Appl Neurophysiol 1982;45:563–72.
Joshi SC, Miller MI. Landmark matching via large deformation diffeomorphisms. IEEE Trans Image Process 2000;9:1357–70.
Kennedy PR, Ross HG. X-ray controlled implantation of the brain stem. J Neurosci Methods 1980;2:411–8.
Kraemer GW, Kemnitz JW, McKinney WT, Howard JL. Use of pneumoencephalography to increase stereotaxic accuracy in rhesus monkeys. Brain Res Bull 1978;3:155–60.
Lewis JW, Van Essen DC. Mapping of architectonic subdivisions in the macaque monkey, with emphasis on parieto-occipital cortex. J Comp Neurol 2000;428:79–111.
Liu Z, Richmond BJ. Response differences in monkey TE and perirhinal cortex: stimulus association related to reward schedules. J Neurophysiol 2000;83:1677–92.
Martin RF, Bowden DM. A stereotaxic template atlas of the macaque brain for digital imaging and quantitative neuroanatomy. Neuroimage 1996;4:119–50.
Miocinovic S, Zhang J, Xu W, Russo GS, Vitek JL, McIntyre CC. Stereotactic neurosurgical planning, recording, and visualization for deep brain stimulation in non-human primates. J Neurosci Methods 2007;162:32–41.
Nahm FK, Dale AM, Albright TD, Amaral DG. In vivo microelectrode localization in the brain of the alert monkey: a combined radiographic and magnetic resonance imaging approach. Exp Brain Res 1994;98:401–11.
Olzewski J. The thalamus of *Macaca mulatta*. An atlas for use with the stereotaxic instruments. Basel, New York: Karger; 1952.
Paton JJ, Belova MA, Morrison SE, Salzman CD. The primate amygdala represents the positive and negative value of visual stimuli during learning. Nature 2006;439:865–70.
Percheron G. Ventricular landmarks for thalamic stereotaxy in *Macaca*. J Med Primatol 1975;4:217–44.
Percheron G, Francois C, Talbi B, Yelnik J, Fenelon G. The primate motor thalamus. Brain Res Rev 1996;22:93–181.
Percheron G, Lacourly N. The lack of precision of thalamic stereotaxy based on Horsley and Clarke cranial coordinates in *Macaca*. Exp Brain Res 1973;18:355–73 [author's transl].
Percheron G, Yelnik J, Francois C. Systems of coordinates for stereotactic surgery and cerebral cartography: advantages of ventricular systems in monkeys. J Neurosci Methods 1986;17:69–88.
Rajkowski J, Kubiak P, Ivanova S, Aston-Jones G. State-related activity, reactivity of locus ceruleus neurons in behaving monkeys. Adv Pharmacol 1998;42:740–4.
Rajkowski J, Majczynski H, Clayton E, Aston-Jones G. Activation of monkey locus coeruleus neurons varies with difficulty and performance in a target detection task. J Neurophysiol 2004;92:361–71.
Rebert CS, Hurd RE, Matteucci MJ, De LaPaz R, Enzmann DR. A procedure for using proton magnetic resonance imaging to determine stereotaxic coordinates of the monkey's brain. J Neurosci Methods 1991;39:109–13.
Risher DW, Zhang X, Kostarczyk E, Gokin AP, Honda CN, Giesler Jr GJ. A method for improving the accuracy of stereotaxic procedures in monkeys using implanted fiducial markers in CT scans that also serve as anchor points in a stereotaxic frame. J Neurosci Methods 1997;73:81–9.
Saunders RC, Aigner TG, Frank JA. Magnetic resonance imaging of the rhesus monkey brain: use for stereotactic neurosurgery. Exp Brain Res 1990;81:443–6.
Schall JD. Decision making: neural correlates of response time. Curr Biol 2002;12:R800–1.
Stanton GB, Deng SY, Goldberg ME, McMullen NT. Cytoarchitectural characteristic of the frontal eye fields in macaque monkeys. J Comp Neurol 1989;282:415–27.
Subramanian T. Cell transplantation for the treatment of Parkinson's disease. Semin Neurol 2001;21:103–15.
Subramanian T, Deogaonkar M, Brummer M, Bakay R. MRI guidance improves accuracy of stereotaxic targeting for cell transplantation in parkinsonian monkeys. Exp Neurol 2005;193:172–80.
Tokuno H, Chiken S. Three-dimensional ultrasonography of monkey brain. Neurosci Res 2004;49:133–8.
Tokuno H, Hatanaka N, Takada M, Nambu A. B-mode and color Doppler ultrasound imaging for localization of microelectrode in monkey brain. Neurosci Res 2000;36:335–8.
Van Essen DC, Dierker DL. Surface-based and probabilistic atlases of primate cerebral cortex. Neuron 2007;56:209–25.
Van Essen DC, Drury HA, Dickson J, Harwell J, Hanlon D, Anderson CH. An integrated software suite for surface-based analyses of cerebral cortex. J Am Med Inform Assoc 2001;8:443–59.
Wagman IH, Loeffler JR, McMillan JA. Relationship between growth of brain and skull of *Macaca mulatta* and its importance for the stereotaxic technique. Brain Behav Evol 1975;12:116–34.
Zeki SM. Functional organization of a visual area in the posterior bank of the superior temporal sulcus of the rhesus monkey. J Physiol 1974;236:549–73.